Preparation and Characterization of Free-standing Hierarchical Porous TiO₂ Monolith Modified with Graphene Oxide

Lei Wan[1], Mingce Long[1*], Dongying Zhou[1], Liying Zhang[2], Weimin Cai[1]

Abstract: Catalyst recovery is one of the most important aspects that restrict the application of TiO₂ photocatalyst. In order to reduce restrictions and improve the photocatalytic efficiency, a hierarchical porous TiO₂ monolith (PTM) with well-defined macroporous and homogeneous mesoporous structure was prepared by using a sol-gel phase separation method. P123 was used as the mesoporous template and graphene oxide was applied to increase the activity and integrity of the monolithic TiO₂. According to scanning electron microscopy and the Barrett-Joyner-Halenda measurements, PTM₃ is mainly composed of 10 nm anatase crystallines with 3.6 nm mesopores and 2-8 μm macropores. Further characterization suggests carbon and nitrogen have been maintained in the PTM during calcinations so as to induce the visible light activity. The PTM with 0.07 wt% graphene oxide dosage shows high efficiency for methyl orange (MO) decolorization under both full spectrum and visible light irradiation ($\lambda > 400$ nm). Besides, the monolith remains intact and has good photocatalytic stability after four cyclic experiments.

Keywords: Photocatalysis; Titanium dioxide; Porous monolith; Graphene oxide

Introduction

Heterogeneous photocatalysis of TiO₂ nanocrystalline is a promising technology to remove recalcitrant toxic organic pollutants in wastewater [1-3]. However, in engineering applications for water purification, catalyst recovery is still a big challenge due to the costly and inefficient separation process for TiO₂ nanoparticles. Efforts have been directed toward immobilization of TiO₂ nanoparticles onto various materials, such as glass, fiber optic cable, plastic, etc [4-8]. However, immobilization will result in a dramatical reduction of surface area and inhibited mass transfer efficiency, therefore, the inherent decrease of catalytic activity blocks

their further scalable application of TiO₂ photocatalysis. Freestanding porous TiO₂ with a large length scale could be a favorable alternative [9,10] because the monolithic structure can be easily separated from aqueous solution and the porous structural characteristic facilitates the mass transfer so as to maintain a feasible reaction rate.

Hierarchically ordered porous structures in natural materials have attracted considerable attention for both fundamental and practical reasons [11,12]. Natural leaves are optimized systems with elaborate hierarchical porous structures and functional components, which play an elaborate crucial role in photosynthesis, including light harvesting, photogenerated charge separation

[1]School of Environmental Science and Engineering, Shanghai Jiao Tong University, Dongchuan Road 800, Shanghai 200240, People's Republic of China
[2]Key Laboratory for Thin Film and Microfabrication of the Ministry of Education, Research Institute of Micro/Nano Science and Technology, Shanghai Jiao Tong University, Shanghai, 200240, China
*Corresponding author. E-mail: Long_mc@sjtu.edu.cn

and catalytic active center for efficient solar energy conversion [13,14]. Inspired by natural materials, several kinds of hierarchical porous TiO_2 replicas have been developed via a two-step infiltration process with leaves [15], egg shells [16] or butterfly wings [17] as templates. However, their methods cannot obtain a large-sized free standing TiO_2 monolith. To the best of our knowledge, little work has been done on free standing hierarchical porous TiO_2 by sol-gel method, because capillary pressure generated during drying treatment makes the TiO_2 sol-gel hard to form intact monolith. Cao et al. obtained free standing and crack free TiO_2-SiO_2 aerogel by drying the precursor with ethanol and CO_2 supercritical method [10,17]. Konishi et al. obtained titania monoliths in a phase-separation method [18,19]. We have developed this method to obtain a monolithic TiO_2 by controlling the amount of water in the precursor, and the resulting catalyst showed efficient activity in water purification [9].

Inspired by the hierarchical porous structure of leaves in the nature, we develop a hierarchical porous TiO_2 monolith with well-defined macroporous and homogeneous mesoporous structure in a sol-gel phase separation method. Graphene is a recent discovery of new 2D nano carbon materials and its strength is the highest of all the materials known so far, so the relevant topics have attracted much attention recently. In our study, graphene oxide (GO) is added to the monolithic TiO_2 and P123 has been used to obtain an ordered porous structure. The dosage of GO is optimized and the photocatalytic performance of the monolithic TiO_2 is tested and characterized.

Experimental sections

Preparation of PTM_x

GO was synthesized from oxidation of graphite by the modified Hummers method [20,21]. In a typical experiment, 0.5 g graphite powder and 0.5 g $NaNO_3$ were introduced to 23 ml concentrated H_2SO_4 in an ice-bath. 3 g $KMnO_4$ was added gradually under vigorous stirring and the temperature of the mixture was maintained below 20℃. The mixture was stirred at 35℃ for 4 h. Then, 46 ml de-ionized water was slowly added into the solution and the mixture was stirred at 98℃ for 15 min. The reaction was terminated by adding 140 ml deionized water and 1 ml H_2O_2 (30 wt%). The resulting graphite oxide was washed with de-ionized water. GO was obtained from the graphite oxide solution by using a JY92-2D ultrasonic crasher (Ningbo Scientz Biotechnology Co. Ltd.) for 40 min. Unexfoliated graphite oxide in suspension after ultrasonication was removed by centrifugation at 3000 rpm for 5 min. The suspension with GO was centrifuged at 8000 rpm for 20 min. The product was dried at 70℃ for 12 h under vacuum

and then re-suspended in water. The obtained suspension with GO (1.3 g/l) was then used for the following synthesis of GO/TiO_2 composites.

Porous TiO_2 monolith was synthesized using a sol-gel method accompanied by phase separation. In a typical procedure, 1.5 ml of acetylacetone was added into 5 ml of tetrabutyl titanate (Ti(OBu)$_4$) under modest stirring and the mixture was named solution A. Another solution composed of 3.2 ml deionized water with 0.2 g P123 and a certain amount of GO dissolved in it was named solution B. Both solution A and solution B were prepared in an ice-bath. Afterwards, 1.86 ml of concentrated HCl was slowly added into solution A, then solution B and 0.17 ml of formamide were successively added dropwise into solution A. The resulting solution was vigorously stirred for 30 min, and then poured into plastic centrifugal tubes, which served as the molds. The sample was aged for one day at 30℃, and finally was dried in an oven at 60℃ for 7 days. The obtained monolithic TiO_2 was carefully taken out and calcined at 350℃ in air, named as PTM_x, wherein x is corresponding to different dosages of GO, that is, 0-3 represent that the GO dosages in the porous TiO_2 monolith are 0 wt%, 0.03 wt%, 0.05 wt% and 0.07 wt%, respectively.

Characterization

The morphology of TiO_2 monolith was observed by a FEI Quanta 250 (20 kV) field emission scanning electron microscope (FESEM). X-ray diffraction (XRD) patterns were recorded on a Rigaku D/Max-2200/PC X-ray diffractometer. The measurements were made on the powder specimens prepared by grinding monolithic TiO_2. X-ray photoelectron spectroscopy (XPS) measurements were carried out on an AXIS Ultra DLD system produced by Kratos company and Shimadu company with Al-K radiation (h=1486.6 eV). UV-vis diffuse reflectance spectra (DRS) were recorded on a Lambda 950 UV/vis spectrophotometer (PerkinElmer Instrument Co., Ltd.) and converted from reflection to absorption by the Kubelka-Munk method. The specific surface area and pore size distribution were measured using a Nova 100 (Quantachrome Instruments) with nitrogen as the adsorption gas, and obtained using the Brunauer-Emmett-Teller (BET) method and the Barrett-Joyner-Halenda (BJH) method, respectively.

Photocatalytic activity

The optical system for photocatalytic activity measurement is composed of a 1000 W xenon lamp and a cutoff filter (λ >400 nm). In a typical test, one or two pieces of intact monolithic TiO_2 were put onto a stainless steel mesh, and 20 mL of methyl orange (MO) solution (initial concentration 10 mg/L) was added into the beaker. The solution with catalyst was stirred in

dark for 30 minutes to reach an adsorption equilibrium. Subsequently the light was switched on, and the sample was taken and analyzed at regular time intervals. The absorbance of MO was monitored with UNICO UV-2101 spectrometer at 464 nm.

The photocatalytic efficiency of the monolithic TiO_2 can be compared by the MO specific removal efficiency (SRE), whose definition is as follows:

$$a = (C_0 - C_t)/C_0 \times t \times m \tag{1}$$

Wherein, C_0 is the initial absorbance of MO, C_t is the absorbance of MO at time t, t is the time when the absorbance of MO decreases to below 15% of C_0, and m is the mass of monolithic TiO_2. Moreover, a_1 corresponds to the SRE under full spectrum irradiation, and a_2 corresponds to the SRE under visible light irradiation ($\lambda >400$ nm).

Results and discussion

Photocatalytic performances of PTM$_x$

The photocatalytic activities of PTM$_x$ have been studied using MO as the model pollutant. As shown in Fig. 1, the photocatalytic performance of PTM$_x$ under visible light irradiation decreases in the order of $PTM_3 > PTM_2 > PTM_1 > PTM_0$ (Fig. 1(a)). Without
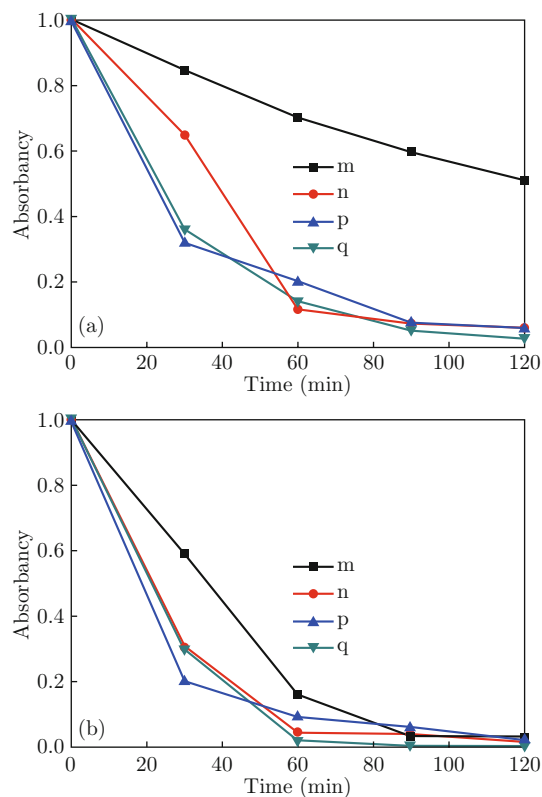

Fig. 1   Photocatalytic degradation of methyl orange over monoliths of (m) PTM$_0$, (n) PTM$_1$, (p) PTM$_2$, (q) PTM$_3$ under visible light (a) and full spectrum (b) irradiation.

addition of GO, the PTM$_0$ also has obvious activity for MO decolorization under both visible light and full spectrum irradiation, however, the structure of the monolith has a slight disruption after reaction. Consequently, from the time dependent curves in Fig. 1, it can be concluded that the sample PTM$_3$ shows better activity for MO removal.

To make the comparison more reasonable, SRE was calculated to evaluate the activities of the PTM$_x$ samples. Figure 2 shows specific removal efficiency of MO over PTM$_x$ under the full spectrum (a$_1$) and visible light irradiation (a$_2$). It can be seen that under visible light irradiation, with addition of graphene oxide, photocatalytic activity was improved as the percentage of graphene oxide increased. As for the full spectrum irradiation, the sample PTM$_2$ shows the best SRE value, a little higher than PTM$_3$. However, the time dependent curves indicate that although the initial decrease of MO is very fast over PTM$_2$, the rate slows down soon, and the final MO removal efficiency is lower than PTM$_3$. Therefore, PTM$_3$ with GO dosage of 0.07 wt% has the highest efficiency for MO decolorization, whose SRE value increases to 4 and 2.2 times of that of PTM$_0$ in the conditions of visible light and full spectrum irradiation, respectively. As is known, the reduced GO is an efficient substrate for electron transfer. Hence, the enhanced photocatalytic activity of the PTM with addition of GO can be attributed to the thermal reduced graphene oxide, which is in favor of photogenerated electron transfer and charge separation [22]. Therefore, taking into account both the activity and structure before and after irradiation, PTM$_3$ has been chosen as the proper photocatalyst for further investigation.
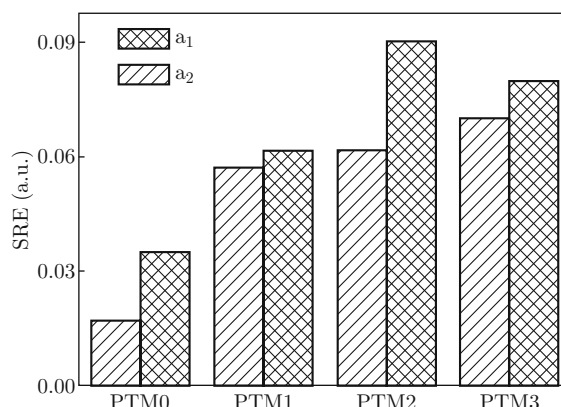

Fig. 2   MO specific removal efficiency (SRE) over PTM$_x$ under full spectrum irradiation (a$_1$) and visible light irradiation (a$_2$).

Characterization of PTM$_3$

Figure 3 shows the XRD patterns of PTM$_3$ and PTM$_0$ samples. In the XRD pattern of PTM$_3$, an intense peak at $2\theta=25.28°$ corresponding to the (101) plane diffraction of anatase TiO_2 is observed and a

smaller peak appears at $2\theta=48.0°$ corresponding to the (200) plane diffraction of anatase TiO_2 [23]. It can be seen that PTM_0 has a similar XRD pattern, but the peak corresponding to the (101) plane diffraction of anatase TiO_2 appears at $2\theta=25.48°$. All diffraction peaks are indexed to pure anatase TiO_2 (JPCDS Card: 84-1286). According to Scherrer's equation, $L_c=K\lambda/(\beta\cos\theta)$ (where λ is the X-ray wavelength, β is the FWHM of the diffraction line, θ is the diffraction angle, and K is a constant, which has been assumed to be 0.9) [24], and according to the full width at half maximum (FWHM) of the peaks at 25.28° and 25.48°, PTM_3 and PTM_0 have an average particle diameter of about 7.2 nm and 7.5 nm, respectively. It reveals that the addition of GO does not affect the crystalline phase of PTM. The result of PTM_3 is strongly consistent with the observation from TEM (Fig. 4). The TEM image manifests that titania particles are almost uniform in a small size (about 8-10 nm). The small dispersed nanoparticles indicate that the TiO_2 monolith consists of small TiO_2 nanoparticles with a quite large specific surface area, which is very important for the photocatalytic performance of PTM_3 sample.
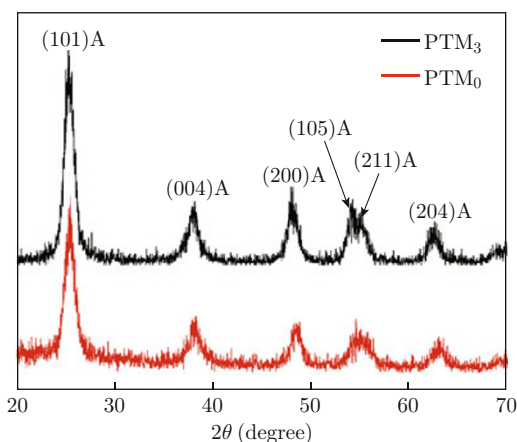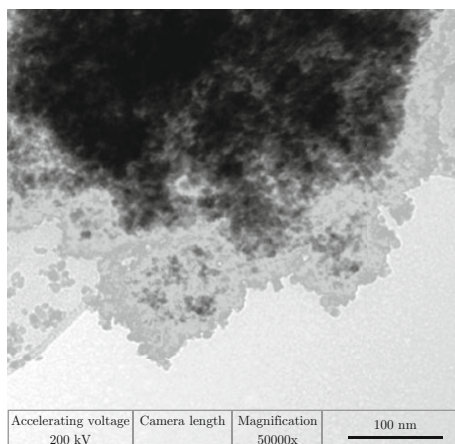
The nitrogen adsorption method is often the first choice used to study the pore characteristics of porous materials [25]. The isotherms (inset graph of Fig. 5) obtained from the nitrogen adsorption-desorption measurements provide information on the surface area and pore size distribution. The pore size distribution is calculated from desorption branch of nitrogen isotherm in the BJH method. Seen from the BJH plots in Fig. 5, PTM_0 exhibits a wide pore-size distribution range centering around 6.5 nm while PTM_3 evidently shifted to the left with a sharp peak at 3.6 nm. The sharp peak indicates that the mesopores are homogeneous in PTM_3. The BET specific surface area of PTM_3 is calculated to be 163 m^2/g, which is more than three times higher than the well-known commercial TiO_2 Degussa P25. However, without addition of GO, the specific surface area of PTM_0 is only 89.6 m^2/g. The result indicates that GO contributes much to the smaller pore size and homogeneous mesopores structure and the enhanced BET specific surface area.
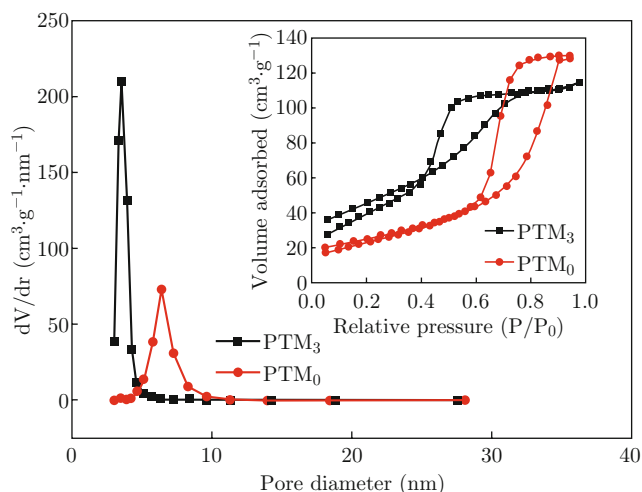

Fig. 3   XRD patterns of PTM_3 and PTM_0.

Fig. 5   BJH pore size distribution plots and N_2 adsorption–desorption isotherms (inset) of PTM_3 and PTM_0.

Fig. 4   TEM image of PTM_3 with magnification of 50000×.

The morphology of PTM_3 can be observed by the SEM images, as shown in Fig. 6. It reveals that the walls of the porous TiO_2 consist of small interconnected TiO_2 nanoparticles with sizes under micrometer scale. Besides, the SEM image with higher magnification (Fig. 6(b)) clearly shows the existence of homogeneous macropores. The macropores are self-organized, originating from the phase separation process. Combining the above analyses of nitrogen adsorption–desorption and XRD, a conclusion can be drawn that PTM_3 is mainly composed of 10 nm anatase crystallines with 3.6 nm mesopores and 2-8 μm macropores. Macropores ensure the light penetration depth and thus improve the efficiency of the light utilization, meanwhile mesoporous and microporous structures guarantee the

large specific surface area and better adsorption ability. Hence, the hierarchical porous structure results in a large BET surface area and good photocatalytic performance [26].
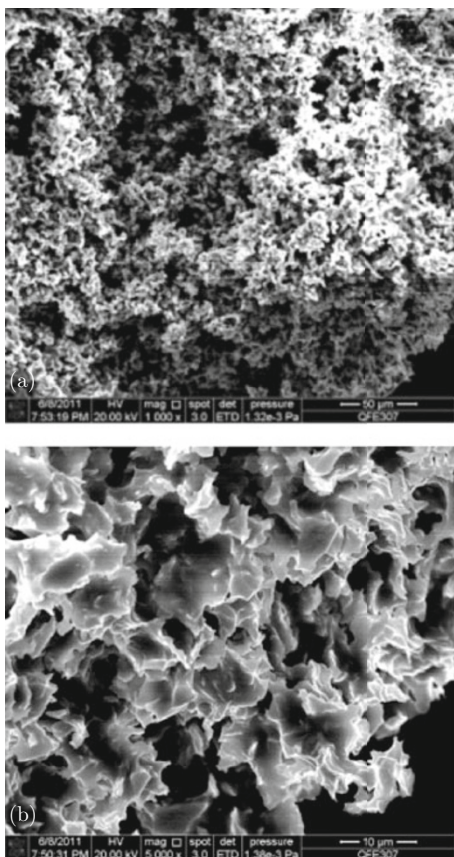

Fig. 6 Typical SEM images of PTM$_3$ calcined at 350℃ with magnification of 1000×(a); with magnification of 5000×(b).

UV-Vis diffuse reflectance spectrum of PTM$_3$ powder is employed to evaluate the optical absorption properties. The measurement is recorded using BaSO$_4$ as a reference, and then the reflectance spectrum is converted into equivalent absorption spectrum by using Kubelka-Munk function (Fig. 7) [27]. It can be seen that PTM$_3$ exhibits an extended optical absorption in both ultraviolet light region and visible light region. The indirect band-gap energy of PTM$_3$ is estimated according to the intercept of the tangent in the plot of $(F(R_\infty)h\nu)^{1/2}$ versus photon energy ($h\nu$). The band-gap energy decreases to 3.02 eV with a threshold wavelength of about 410 nm, which is narrower than that of anatase TiO$_2$ (about 3.2 eV) [28], as shown in Fig. 6. The extended visible light absorption can be supported by the highly efficient decoloarization of MO solution under visible light irradiation, which is attributed to the incorporation of carbon and nitrogen species. Moreover, the long tail in the region till 800 nm is also

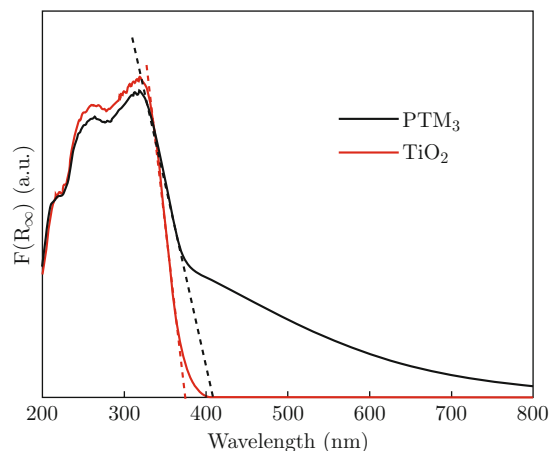observed, indicating the presence of surface modified species.

Fig. 7 UV-vis absorption spectra of PTM$_3$ and commercial anatase TiO$_2$.

To further investigate chemical states of the existence of carbon and nitrogen elements in the PTM$_3$, XPS has been measured, as shown in Fig. 8. The binding energies are all calibrated by using the contaminant carbon at binding energy of 284.8 eV. From the high resolution core-level spectra of titanium, two peaks at 464.6 eV and 463.8 eV (Fig. 8(a)) can be seen, which are ascribed to the Ti2p3/2 and Ti2p1/2 of TiO$_2$ [29]. However, there is also a small peak at 461.3 eV, and we tentatively ascribe this peak to the Ti^{3+}, which might be related with oxygen vacancy, and contributes much to the visible light activity of TiO$_2$ [30]. The peaks at 529.9 eV and 532.1 eV in Fig. 8(b) are attributed to the bulk O$_2$ from TiO$_2$ and –OH adsorbed on the surface of PTM$_3$, respectively [29]. The larger area at 532.1 eV indicates the abundance of surface states.

The high resolution C1s core-level XPS spectrum is shown in Fig. 8(c). The first peak at 284.8 eV arises from the adventitious carbon contamination and the other two peaks at 286.0 eV and 288.4 eV suggest the existence of C-O and C=O bonds, respectively, which indicates the formation of carbonated species [31]. Fig. 8(d) shows the high resolution N1s core-level XPS spectrum, which could be deconvoluted into two peaks (401.7 eV and 403.4 eV). The main peak at 401.7 eV corresponds to the N atoms that replace the O atoms inside of the TiO$_2$ [32]. Another peak at 403.4 eV can be attributed to the N-O bond over the surface of TiO$_2$ powder [33]. Considering that PTM$_3$ presents only the anatase phase in the XRD spectra, it can be inferred that some compounds containing nitrogen or carbon form over the TiO$_2$ surface and consquently increase the absorption ability of TiO$_2$monolith for visible light.
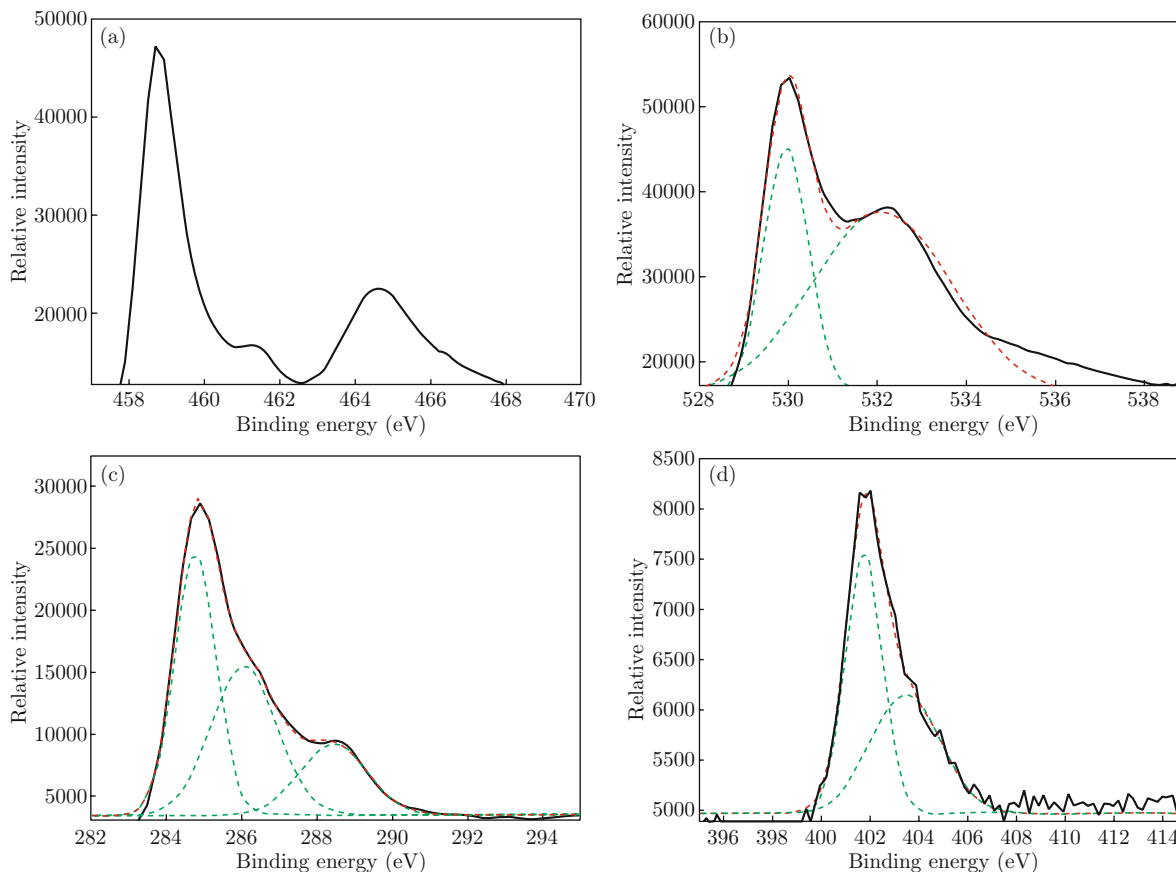
Fig. 8   XPS spectra for PTM$_3$: (a) Ti2p, (b) O1s, (c) C1s, and (d) N1s.

Photocatalytic stability and structural integrity

To evaluate the photocatalytic stability of the PTM$_3$ catalyst, cyclic experiments are conducted, as shown in Fig. 9. In each test, one small piece of PTM$_3$ was
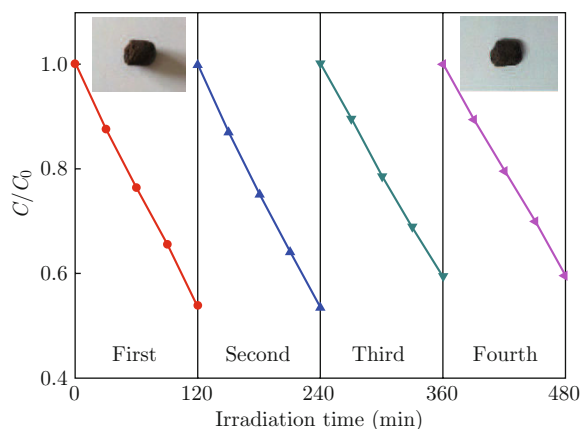

Fig. 9 Cycling runs in photocatalytic degradation of methyl orange (insets are the digital pictures of the PTM$_3$ before and after four cycling tests).

applied as the catalyst, and the MO solution with a same initial concentration is illuminated under visible light for 2 h. We can see that after the first two rounds

of the experiments, the photocatalytic activity of PTM$_3$ shows a slight decline. It is probably because that during photocatalytic degradation, some of the intermediate products adsorbed inside the catalyst and reduced the photocatalytic activity. In the following continuous tests, PTM$_3$ shows a stable photocatalytic performance in the cyclic experiments. Moreover, the digital pictures of PTM$_3$ before and after the degradation (inset pictures of Fig. 9) show that the structure of the PTM$_3$ catalyst remains intact after the cyclic experiments. In another control test, the absorbance of methyl orange has almost no change after two-hour irradiation in the absence of catalysts.

Consequently, by selecting a proper template and optimizing the synthesis parameters, it is promising to prepare a 3D monolithic material with structure similar to leaves in the nature. This material has a good application prospect in water purification, because it can keep an intact structure under a flowing media, consequently avoiding the complex steps like recovery or immobilization of photocatalysts.

Conclusion

Hierarchical porous TiO$_2$ monoliths with high photocatalytic activity have been successfully synthesized in

a sol-gel method accompanied by phase separation. The TiO_2 monolith is mainly composed of 10 nm anatase crystallines, and has a hierarchical porous structure with 3.6 nm mesopores and 2-8 μm macropores. P123 and GO play an important role in structural integrity and stability of the monolith, and the pore size can be tailored by adjusting the starting compositions. Due to the macroporous and homogeneous mesoporous structure, the BET specific surface area can reach 163 m^2/g. The porous TiO_2 monolith remains intact after being applied for the discolorization of MO solution. Therefore, it has a promising prospect in applications of photocatalytic water purification, mesoporous membranes, etc.

Acknowledgements

References

[1] M. R. Hoffmann, S. T. Martin, W. Choi and D. W. Bahnemann, Chem. Rev. 95, 69 (1995). http://dx.doi.org/10.1021/cr00033a004

[2] A. Fujishima, X. Zhang and D. A. Tryk, Surf. Sci. Rep. 63, 515 (2008). http://dx.doi.org/10.1016/j.surfrep.2008.10.001

[3] M. C. Long and W. M. Cai, Front. Chem. Chin. 6, 190 (2011). http://dx.doi.org/10.1007/s11458-011-0243-8

[4] J. G. Yu, H. G. Yu, C. H. Ao, S. C. Lee, J. C. Yu and W. K. Ho, Thin Solid Films 496, 273 (2006). http://dx.doi.org/10.1016/j.tsf.2005.08.352

[5] H. Han and R. B. Bai, Ind. Eng. Chem. Res. 50, 11922 (2011). http://dx.doi.org/10.1021/ie200787j

[6] D. D. Dionysiou, A. A. Burbano, M. T. Suidan, I. Baudin and J. M. Laine, Environ. Sci. Technol. 36, 3834 (2002). http://dx.doi.org/10.1021/es0113605

[7] N. J. Peill and M. R. Hoffmann, Environ. Sci. Technol. 30, 2806 (1996). http://dx.doi.org/10.1021/es960047d

[8] G. L. Puma, J. N. Khor and A. Brucato, Environ. Sci. Technol. 38, 3737 (2004). http://dx.doi.org/10.1021/es0301020

[9] C. Chen, W. M. Cai, M. C. Long, J. Y. Zhang, B. X. Zhou, Y. H. Wu and D. Y. Wu, J. Hazard. Mater. 178, 560 (2010). http://dx.doi.org/10.1016/j.jhazmat.2010.01.121

[10] S. Cao, N. Yao and K. L. Yeung, J. Sol-Gel Sci. Technol. 46, 323 (2008). http://dx.doi.org/10.1007/s10971-008-1701-8

[11] F. Xia and L. Jiang, Adv. Mater. 20, 2842 (2008). http://dx.doi.org/10.1002/adma.200800836

[12] G. Calzaferri, Top. Catal. 53, 130 (2009). http://dx.doi.org/10.1007/s11244-009-9424-9

[13] H. Zhou, X. Li, T. Fan, F. E. Osterloh, J. Ding, E. M. Sabio, D. Zhang and Q. Guo, Adv. Mater. 22, 951 (2010). http://dx.doi.org/10.1002/adma.200902039

[14] X. Li, T. Fan, H. Zhou, S. K. Chow, W. Zhang, D. Zhang, Q. Guo and H. Ogawa, Adv. Funct. Mater. 19, 45 (2009). http://dx.doi.org/10.1002/adfm.200800519

[15] D. Yang, L. Qi and J. Ma, Adv. Mater. 14, 1543 (2002). http://dx.doi.org/10.1002/1521-4095

[16] W. Zhang, D. Zhang, T. Fan, J. Gu, J. Ding, H. Wang, Q. Guo and H. Ogawa, Chem. Mater. 21, 33 (2009). http://dx.doi.org/10.1021/cm702458p

[17] S. Cao, K. L. Yeung and P. L. Yue, Appl. Catal. B-Environ. 68, 99 (2006). http://dx.doi.org/10.1016/j.apcatb.2006.07.022

[18] J. Konishi, K. Fujita, K. Nakanishi and K. Hirao, Chem. Mater. 18, 6069 (2006). http://dx.doi.org/10.1021/cm0617485

[19] J. Konishi, K. Fujita, K. Nakanishi and K. Hirao, Chem. Mater. 18, 864 (2006). http://dx.doi.org/10.1021/cm052155h

[20] W. S. Hummers and R. E. Offeman, J. Am. Chem. Soc. 80, 1339 (1958). http://dx.doi.org/10.1021/ja01539a017

[21] C. Chen, W. M. Cai, M. C. Long, B. X. Zhou, Y. H. Wu, D. Y. Wu and Y. J. Feng, ACS Nano 4, 6425 (2010). http://dx.doi.org/10.1021/nn102130m

[22] X. An and J. C. Yu, RSC Adv. 1, 1426 (2011). http://dx.doi.org/10.1039/C1RA00382H

[23] J. G. Yu, Y. R. Su and B. Cheng, Adv. Funct. Mater. 17, 1984 (2007). http://dx.doi.org/10.1002/adfm.200600933

[24] L. S. Birks and H. Friedman, J. Appl. Phys. 17, 687 (1946). http://dx.doi.org/10.1063/1.1707771

[25] X. C. Wang, J. C. Yu, C. M. Ho, Y. D. Hou and X. Z. Fu, Langmuir 21, 2552 (2005). http://dx.doi.org/10.1021/la047979c

[26] G. C. Groen, L. A. A. Peffer and J. Pérez-Ramírez, Micropor. Mesopor. Mater. 60, 1 (2003). http://dx.doi.org/10.1016/s1387-1811(03)00339-1

[27] M. C. Long, J. J. Jiang, Y. Li, R.Q. Cao, L. Y. Zhang and W. M. Cai, Nano-Micro Lett. 3, 171 (2011). http://dx.doi.org/10.5101/nml.v3i3.p171-177

[28] J. Grzechulska and A. W. Morawski, Appl. Catal. B-Environ. 46, 415 (2003). http://dx.doi.org/10.1016/S0926-3373(03)00265-0

[29] Y. Xie, X. J. Zhao, Y. X. Chen, Q. N. Zhao and Q. H. Yuan, J. Solid State Chem. 180, 3576 (2007). http://dx.doi.org/10.1016/j.jssc.2007.10.023

[30] F. Zuo, L. Wang, T. Wu, Z. Y. Zhang, D. Borchardt and P. Y. Feng, J. Am. Chem. Soc. 132, 11856 (2010). http://dx.doi.org/10.1021/ja103843d

[31] D. M. Chen, Z. Y. Jiang, J. Q. Geng, Q. Wang and D. Yang, Ind. Eng. Chem. Res. 46, 2741 (2007). http://dx.doi.org/10.1021/ie061491k

[32] J. Casanovas, J. M. Ricart, J. Rubio, F. Illas and J. M. Jimenez-Mateos, J. Am. Chem. Soc. 118, 8071 (1996).

http://dx.doi.org/10.1021/ja960338m

[33] A. E. Aleksenskii, V. Y. Osipov, A. Y. Vul', B. Y. Ber, A. B. Smirnov, V. G. Melekhin, G. J. Adriaenssens and K. Iakoubovskii, Phys. Solid State 43, 145 (2001). http://dx.doi.org/10.1134/1.1340200